Strain-engineering of magnetic anisotropy in Co_xNi_{1-x}-$SrTiO_3/SrTiO_3(001)$ vertically assembled nanocomposites

Xiaorong Weng,[1,*] Marcel Hennes,[1] Amélie Juhin,[2] Philippe Sainctavit,[2] Benoit Gobaut,[3,†] Edwige Otero,[3]
Fadi Choueikani,[3] Philippe Ohresser,[3] Thomas Tran,[1] David Hrabovsky,[4] Dominique Demaille,[1]
Yunlin Zheng,[1] and Franck Vidal[1,‡]
[1]*Sorbonne Université, CNRS, Institut des NanoSciences de Paris, INSP, UMR7588, F-75005 Paris, France*
[2]*Sorbonne Université, CNRS, Institut de Minéralogie, de Physique des Matériaux et de Cosmochimie, IMPMC, UMR7590, F-75005 Paris, France*
[3]*Synchrotron SOLEIL, L'Orme des Merisiers Saint-Aubin BP 48, 91192 Gif-sur-Yvette Cedex, France*
[4]*Sorbonne Université, Mesures Physiques à Basses Températures, F-75005 Paris, France*

(Received 7 February 2022; accepted 22 March 2022; published 4 April 2022)

Ultrathin Co_xNi_{1-x} alloy nanowires vertically embedded in $SrTiO_3/SrTiO_3$ (001) thin films were grown using a self-assembly approach based on sequential pulsed laser deposition. Due to vertical epitaxial coupling of the metallic and oxide phases, a large average tensile strain of up to 4% arises within the nanowires, which is evidenced using a combination of x-ray diffraction and transmission electron microscopy. Macroscopic magnetometry experiments are used to demonstrate that this huge deformation allows us to enhance the uniaxial anisotropy of the nanowires, leading to saturation field in excess of 1 T in the hard direction, large coercive field at low temperature along the easy axis, and to a blocking temperature exceeding 600 K in the case of nanowires with a diameter of 5 nm and 78% Co content. These data are complemented with angular dependent x-ray magnetic circular dichroism measurements at the Co and Ni $L_{2,3}$ edges. The value of the magnetic moment was extracted from these measurements by applying sum rules and the anisotropy of the orbital moment was investigated.

DOI: 10.1103/PhysRevMaterials.6.046001

I. INTRODUCTION

Accurate control of the magnetization direction is a key aspect in existing or emerging technologies for magnetic data storage and processing. In such a context, the development of new nanostructured materials requires fundamental studies exploring routes to tailor the magnetic anisotropy that determines the direction and the thermal stability of the magnetization. Strain-engineering is an appealing strategy that can be employed in order to enhance the magnetic anisotropy. While this approach has been used extensively in the case of continuous thin and ultrathin films [1], less work has been devoted to the control of magnetic properties via strain in isolated nano-objects. Recently, vertically assembled nanostructures (VANs) [2] were demonstrated to possess great potential for the development of systems with tailored magnetic anisotropies. As illustrated in Fig. 1, the geometry and the epitaxial character of these composites can be used to control the distinct sources of magnetic anisotropy in embedded nano-objects. The competition/synergy between magnetoelastic and magnetostatic contributions has already been studied in all-oxide VANs, particularly in the case of layers hosting nanopillars made of $CoFe_2O_4$, a piezomagnetic compound [3–8]. In contrast, hybrid metal-oxide VANs have been less explored so far [9,10]. In earlier studies, we have evidenced large magnetoelastic effects in Ni-$SrTiO_3$ VANs [11,12]. From a quantitative perspective, the uniaxial magnetic anisotropy has two sources in this system: (i) a magnetostatic term, or shape anisotropy, given by $K_{ms} = K_{ms}^{(1)} \sin^2 \alpha$ with α being the angle between the axis of the wires and the magnetization and $K_{ms}^{(1)} = \mu_0 M_s^2/4$ with M_s the saturation magnetization density, and (ii) the magnetoelastic anisotropy that is given by $K_{me} = K_{me}^{(1)} \sin^2 \alpha$ with

$$K_{me}^{(1)} = \frac{3}{2}\lambda_{001}(c_{11} - c_{12})(\epsilon_{zz} - \epsilon_{rr}). \qquad (1)$$

In this equation, c_{ij} are elastic constants, ϵ_{zz} is the strain along [001] (axial strain), ϵ_{rr} is the radial strain, and λ_{001} is the magnetostriction coefficient. As λ_{001} is negative in pure Ni, large axial strains eventually lead to a negative value of $K_{ms}^{(1)} + K_{me}^{(1)}$ and the axis of the wires becomes a magnetic hard axis [12].

In the bulk Co_xNi_{1-x} binary system, the amplitude and sign of the magnetostriction coefficient λ_{001} varies with the composition x of the alloy. Starting from a negative value for pure Ni, its amplitude drops as x increases up to 0.2. At $x = 0.2$, $\lambda_{001} = 0$. For $x > 0.2$, λ_{001} is positive and increases with x [13]. This yields an appealing path for perpendicular magnetic anisotropy enhancement. Provided that the face-centered

---

[*] Present address: Université Grenoble Alpes, CEA, IRIG/DePhy/MEM/CNRS, 38054 Grenoble, France.

[†] Present address: Université de Strasbourg, CNRS, Institut de Physique et Chimie des Matériaux de Strasbourg, UMR 7504, F-67000 Strasbourg, France.

[‡] franck.vidal@sorbonne-universite.fr

cubic structure of the Co_xNi_{1-x} alloy is preserved and that large axial strains can be achieved, the combined contributions of $K_{ms}^{(1)}$ and $K_{me}^{(1)}$ are expected to result in a large uniaxial anisotropy. We examine this strategy in the present paper on a macroscopic and microscopic scale combining structural and magnetometry measurements. These data are complemented by XMCD experiments. Using the well established sum rules [14,15], we calculate spin and orbital magnetic moments and thereby provide a quantitative, element-selective description of their angular dependence. We eventually use Bruno's model [16] to link the macroscopically observed anisotropy energy with the anisotropy of the orbital moment. The paper is organized as follows: after a first part devoted to the description of the experimental techniques used in this work, we will give detailed insight into the structural characteristics of the samples before turning to an in-depth analysis of their magnetic properties.

II. SAMPLE GROWTH AND ANALYSIS

A. Growth

Co_xNi_{1-x} (CoNi) nanowires embedded in a $SrTiO_3$ matrix were grown by sequential pulsed laser deposition (PLD) of cobalt, nickel, and $SrTiO_3$ (STO) on Nb-doped $SrTiO_3(001)$ and $SrTiO_3(001)$ substrates, following procedures established previously to synthesize Co, Ni, and CoNi nanowires in $CeO_2/SrTiO_3$, $(Sr, Ba)TiO_3$, and $SrTiO_3$ [11,12,17–31]. A quadrupled Nd:YAG laser (wavelength 266 nm) operating at 10 Hz and a fluence in the 1–3 J/cm^2 range was used. The growth temperature was 650 °C. The composition of the Co_xNi_{1-x} alloy was set by adjusting the growth sequence following procedures similar to the ones described in Ref. [23]. In the rest of this paper the samples will be named as $S\xi\zeta$ with the number $\xi\zeta$ being equal to the percentage of Co in the CoNi alloy. Samples S00, S18, S57, and S78 were grown using the same temperature and laser fluence on Nb-doped $SrTiO_3(001)$. S80 was grown at slightly lower temperature and laser fluence on $SrTiO_3(001)$. Following the sequential deposition step, the samples were capped with a ~3-nm-thick Al_2O_3 layer in order to protect them against contamination and avoid NW oxidation.

B. Structural measurements

The structure of the samples was studied using a combination of techniques including transmission electron microscopy (TEM) and x-ray diffraction (XRD). High resolution transmission electron microscopy (HRTEM) data were acquired using a JEOL JEM 2100F equipped with a field-emission gun operated at 200 kV and a Gatan GIF spectrometer. XRD data were collected on a laboratory 5-circles diffractometer (Rigaku SmartLab) with Cu K_α radiation (wavelength of 1.54 Å) in order to determine the epitaxial relationship in the nanocomposites. The mean axial strain in the CoNi wires was determined through the analysis of θ-2θ scans. The diffraction intensity is given as a function of reciprocal lattice units (r.l.u) in what follows with $SrTiO_3$ reciprocal basis as a reference.

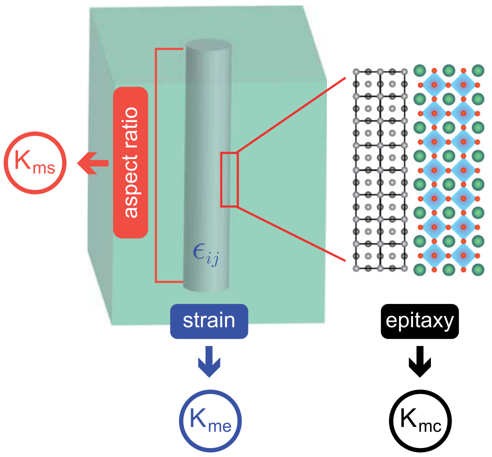

FIG. 1. Control of magnetic anisotropies in vertically assembled nanostructures: the shape of embedded nanopillars determines the magnetostatic anisotropy K_{ms}, the strain leads to a magnetoelastic contribution K_{me}, and the epitaxial relationship sets the easy and hard axes related to the magnetocrystalline anisotropy K_{mc}.

C. Magnetometry measurements

Magnetic measurements were performed using a vibrating sample magnetometer (VSM) option in a physical properties measurement system (Quantum Design PPMS 9T). The magnetization M was measured as a function of the applied magnetic field in out-of-plane and in-plane geometries. The magnetic hysteresis cycles were corrected by removing the diamagnetic signal (obtained by extrapolating the linear slope of the curves at large magnetic fields) in order to extract the ferromagnetic part corresponding to the response of the NWs assembly. First-order reversal curves (FORCs) were collected at $T = 5$ K according to the protocol of Pike [32]. The field was applied along the axis of the nanowires. Saturation field was applied prior to every reversal. The reversal field was decreased by -0.03 T steps. FORC data were processed with the *FORCinel* software [33]. The FORC technique is used in order to retrieve the distribution of switching fields corrected from the dipolar interaction between wires.

D. Spectroscopic measurements

X-ray absorption spectroscopy (XAS) and x-ray magnetic circular dichroism (XMCD) experiments were performed on the DEIMOS beamline of SOLEIL synchrotron [34–36]. The samples were kept under ultrahigh vacuum at 4.2 K during measurements. Data were acquired in total electron yield (TEY) mode. The applied magnetic field $\mu_0\vec{H}$ was collinear to the x-ray propagation vector $\vec{k}$. The incidence on the sample was set through a rotation of the sample by an angle γ, as described in Fig. 2 where $\gamma = 0^\circ$ refers to normal incidence. XAS and XMCD spectra were acquired at the Co and Ni $L_{2,3}$ edges by scanning the photon energy in the 760–830 and 840–880 eV ranges. We use the following notations for combinations of magnetic field orientation and circular polarization: μ^+ corresponds to $\mu_0\vec{H}$ parallel to $\vec{k}$ for left circular polarization and to $\mu_0\vec{H}$ antiparallel to $\vec{k}$ for right circular polarization, μ^- corresponds to $\mu_0\vec{H}$ parallel to $\vec{k}$ for right

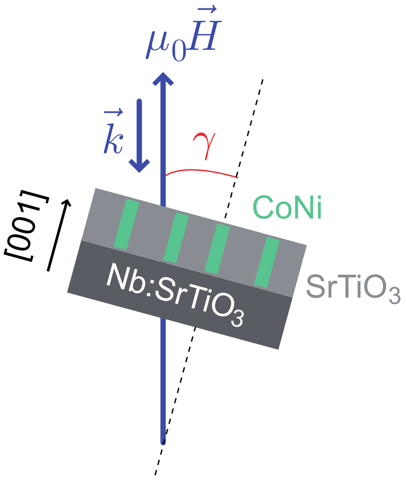

FIG. 2. Geometry used for XMCD measurements. $\vec{k}$ is the wave vector of soft x rays, parallel to the applied magnetic field. γ is the angle between $\vec{k}$ and the surface normal.

circular polarization and to $\mu_0\vec{H}$ antiparallel to $\vec{k}$ for left circular polarization. Element-specific hysteresis loops were acquired by scanning the magnetic field at constant x-ray energy, set to the maximum of the XMCD signal. For the acquisition of XMCD spectra at remanence the samples were submitted to a magnetic field exceeding the saturation field in the positive direction, the field was then set to zero and absorption spectra were recorded with left and right circular polarizations. The same procedure was then applied with the saturating field in the opposite direction. The XMCD spectra at remanence were obtained by properly averaging data recorded for both directions of application of the field.

III. FORMATION, EPITAXY, AND STRAIN STATE OF NANOWIRES

A. Diameter, density, and chemical composition

The formation of the CoNi-SrTiO$_3$ VANs was studied using electron transmission microscopy as in the case of similar systems explored previously [30]. Figure 3(a) shows a cross-sectional view of the S57 sample. The formation of columnar nanostructures is evident from the presence of elongated (in the [001] direction), ~5-nm-wide zones with moiré patterns. Plan view imaging was used in order to determine the mean diameter of the CoNi nanowires in the VANs. The composition $\xi\zeta$ was determined quantitatively by energy dispersive spectroscopy during TEM measurements. The results are displayed in Table I. As can be seen, the series of nanocomposites studied here consists of four samples with a mean nanowire diameter of ~5 nm and varying composition of the CoNi alloy (S00, S18, S57, S78) as well as a sample with 80% Co and smaller mean diameter of the nanowires.

B. Epitaxy and strain

The inset in Fig. 3(a) shows the fast Fourier transform (FFT) of the cross sectional TEM view. Indexing the FFT reveals a cube-on-cube epitaxy of face-centered cubic CoNi in the SrTiO$_3$ matrix, as shown by the positions of the 111 and 002 spots marked by arrows. Cube-on-cube epitaxial alignment and the fact that CoNi remains in the face-centered cubic structure were confirmed by TEM plan view imaging and x-ray diffraction measurements. θ-2θ scans were used in order to determine the axial strain ϵ_{zz} in the nanowires. As shown in Fig. 3(b), the 002 reflection of CoNi is shifted towards lower ℓ values with respect to the expected position

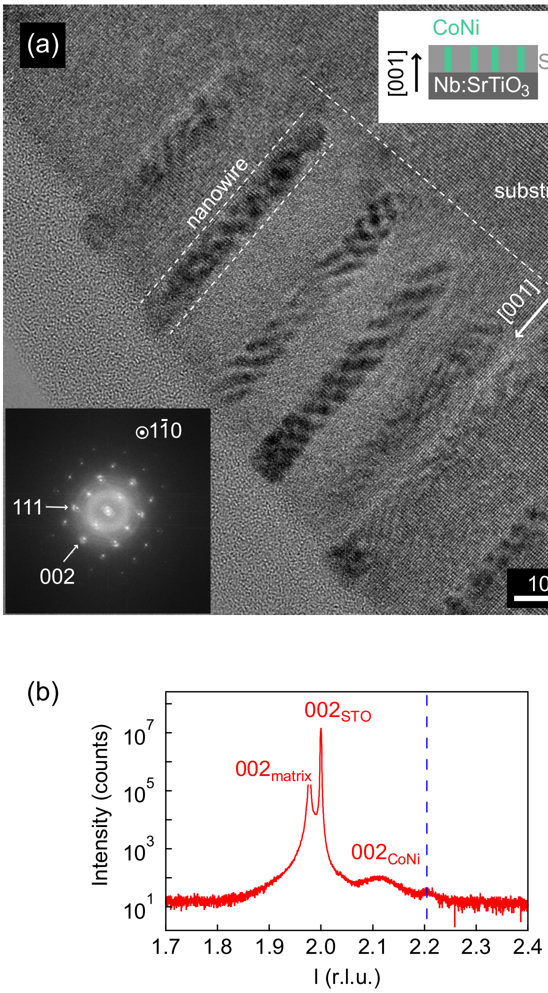

FIG. 3. (a) High resolution TEM cross section of the S57 sample, acquired along the 1$\bar{1}$0 zone axis. Upper inset: Schematics of the sample. Lower inset: Fourier transform of the image. (b) θ-2θ scan of sample S78. The dashed vertical line indicates the position of the Bragg reflection of the unstrained bulk CoNi alloy.

TABLE I. Structural parameters deduced from TEM and XRD analysis of the nanocomposites. $\langle D\rangle$: mean diameter of the NWs, ρ: in-plane density of the NWs, t: epilayer thickness, $\langle\epsilon_{zz}\rangle$: mean axial strain.

Sample	% Co	$\langle D\rangle$ (nm)	ρ (cm^{-2})	t (nm)	$\langle\epsilon_{zz}\rangle$ (%)
S00	0	5.0	5.1×10^{11}	106	2.4
S18	18	5.3	4.5×10^{11}	110	2.8
S57	57	5.0	3.9×10^{11}	113	3.1
S78	78	5.0	4.3×10^{11}	106	4.2
S80	80	3.4	1.3×10^{12}	60	5.0

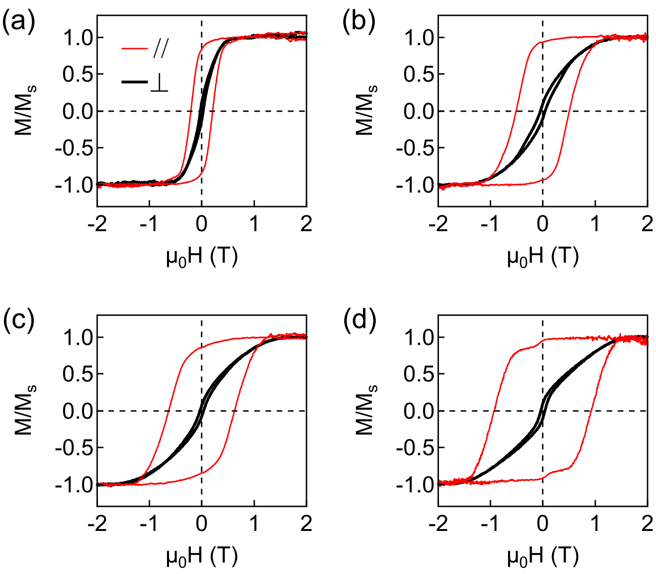

FIG. 4. Magnetic hysteresis cycles recorded at $T = 10$ K with the applied magnetic field along the axis of the nanowires (thin line) and perpendicular to it (thick black line) for samples S18 (a), S57 (b), S78 (c), and S80 (d).

for an unstrained bulk alloy. This corresponds to a large value of ϵ_{zz}, of several percent. Such a large strain, arising from the epitaxial nature of the VANs, was measured for every sample in the series with diameter around 5 nm. θ-2θ scans for the set of samples studied can be found in Ref. [37]. The results of the strain measurements are summarized in Table I. Finally, it should be noted that the out-of-plane lattice parameter of the matrix is larger than that of the substrate, as shown by the peak at $l = 1.977$. This is a consequence of the nonstoichiometry of $SrTiO_3$ when growth is carried out in an oxygen-free atmosphere [38–40].

IV. MAGNETIC PROPERTIES

A. Magnetic anisotropy

Figure 4 shows magnetic hysteresis cycles recorded at $T = 10$ K with the applied magnetic field parallel and perpendicular to the axis of the nanowires for samples S18, S57, S78, and S80. In every sample, the loop acquired with the field applied along the axis of the nanowires exhibits a much more pronounced squareness than the loop acquired with the field applied perpendicular to the axis. In the case of S80, the normalized remanence M_r/M_s reaches 0.92 and the coercive field reaches 0.93 T. In contrast, the cycles obtained when applying the field in the plane of the VAN thin films are nearly closed with large values of the saturation field.

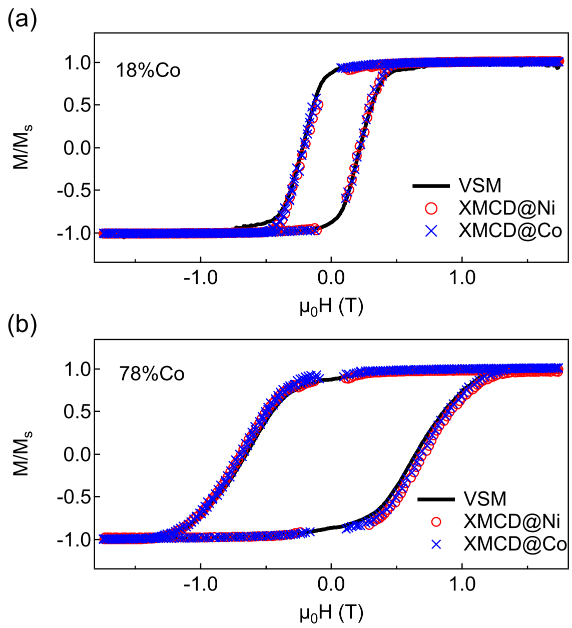

FIG. 5. Magnetic hysteresis cycles measured with the field applied along the axis of the nanowires ($\gamma = 0$) by XMCD at the Ni $L_{2,3}$ edges (circles) and Co $L_{2,3}$ edges (crosses) at $T = 4.2$ K, and by VSM (line) at $T = 5$ K. (a) Data for S18 sample. (b) Data for S78 sample.

As illustrated in Fig. 5, cyclic magnetometry experiments, performed by XMCD and by extraction magnetometry, yield the same response, as shown for two different concentrations at the Co and Ni L edges (field applied along the nanowires axis). Only small differences are observed, which may be ascribed to the fact that the VSM signals were obtained at $T = 5$ K while XMCD measurements were performed at $T = 4.2$ K. Taken together, these data highlight that the XMCD measurements, despite being performed in TEY mode, are representative of the global response of the wires.

Cyclic magnetometry indicates that the magnetic anisotropy of the VANs is dominated by a uniaxial magnetic anisotropy with an easy axis oriented along the backbone of the wires. This is confirmed by measurements of M_r/M_s as a function of γ, shown in Fig. 6, for samples S18 and S78. The fact that M_r/M_s is maximal for $\gamma = 0$ and the $\cos\gamma$-like variation are characteristic of a uniaxial magnetic anisotropy with easy axis along the [001] direction. In the case of VANs hosting pure Ni nanowires, the [001] direction was found to be the hard axis [11,12]. This was traced back to the negative uniaxial magnetoelastic anisotropy arising from the large axial strain in the wires. In the case of CoNi nanoalloy wires, the magnetoelastic contribution should lead

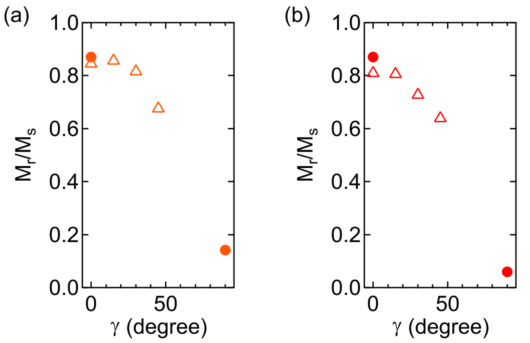

FIG. 6. Normalized remanence measured as a function of the angle γ between [001] and the applied magnetic field by XMCD at the Ni $L_{2,3}$ edges at $T = 4.2$ K (open triangles) and VSM at $T = 5$ K (solid disks). (a) Results for S18 sample. (b) Results for S78 sample.

TABLE II. First two columns: calculated saturation magnetization M_s and shape anisotropy field $\mu_0 H_a^{\mathrm{ms}}$ of CoNi alloys with compositions corresponding to the samples S18, S57, S78, and S80. Third and fourth columns: measured coercive field $\mu_0 H_c$ at $T = 10$ K and saturation field in the hard plane $\mu_0 H_s^{\perp}$.

Composition	M_s (A/m)	$\mu_0 H_a^{\mathrm{ms}}$ (T)	$\mu_0 H_c$ (T)	$\mu_0 H_s^{\perp}$ (T)
$Co_{0.18}Ni_{0.82}$	6.74×10^5	0.42	0.21	0.55±0.05
$Co_{0.57}Ni_{0.43}$	10.35×10^5	0.65	0.50	1.4±0.1
$Co_{0.78}Ni_{0.22}$	12.30×10^5	0.77	0.63	1.6±0.1
$Co_{0.80}Ni_{0.20}$	12.50×10^5	0.78	0.93	1.7±0.1

to an enhancement of the positive uniaxial anisotropy for Co contents above 18%. We will now address this issue.

Table II gives the bulk values of M_s for Co_xNi_{1-x} alloys with concentrations equal to the ones studied here.

From M_s, $K_{\mathrm{ms}}^{(1)} = \frac{\mu_0}{4} M_s^2$ and the associated anisotropy field $\mu_0 H_a^{\mathrm{ms}} = 2K_{\mathrm{ms}}^{(1)}/M_s = \mu_0 M_s/2$ can be obtained straightforwardly. The values of $\mu_0 H_a^{\mathrm{ms}}$ are listed in Table II for the alloy compositions studied in this paper. These values are compared to the measured saturation fields in the hard plane $\mu_0 H_s^{\perp}$, and to the coercive field $\mu_0 H_c$. Since $\alpha = \pi/2$ defines the hard magnetic plane of the VANs, the value of $\mu_0 H_s^{\perp}$ provides a good estimation of the total anisotropy field of the systems. Therefore, the results displayed in Table II indicate that the anisotropy field is enhanced for S57, S78, and S80, compared to what is expected when shape is the only source of uniaxial magnetic anisotropy. In the case of S18, the anisotropy field is close to $\mu_0 H_a^{\mathrm{ms}}$. The enhancement of the uniaxial anisotropy is further substantiated by the large value of the coercive field of the S80 VAN for which $\mu_0 H_c = 0.93$ T is measured at $T = 10$ K. Since the upper value for the coercive field at low T is given by the anisotropy field, the fact that $\mu_0 H_c$ exceeds $\mu_0 H_a^{\mathrm{ms}}$ for S80 is strong proof for magnetic anisotropy enhancement.

As stated in the Introduction, large axial strains along the backbone of the CoNi nanowires should lead to sizable uniaxial magnetoelastic anisotropies for Co-rich compositions. For S18, with λ_{001} expected to be close to zero [13], the magnetoelastic effect should be less prominent than for larger Co contents where a large enhancement is possible. Using the relation between the anisotropy field and the uniaxial magnetic anisotropy $\mu_0 H_a = 2K^{(1)}/M_s$ and assuming that $\mu_0 H_a \simeq \mu_0 H_s^{\perp}$, we can estimate the total uniaxial anisotropy $K^{(1)}$ and the magnetoelastic anisotropy given by $K_{\mathrm{me}}^{(1)} = K^{(1)} - K_{\mathrm{ms}}^{(1)}$. For S18, we obtain $K^{(1)}/K_{\mathrm{ms}}^{(1)} \simeq 1.3$, while this ratio is larger than 2 for all other samples. The largest ratio is obtained for S80 with $K^{(1)}/K_{\mathrm{ms}}^{(1)} \simeq 2.5$. Therefore, our measurements are fully consistent with a magnetoelastic origin of the magnetic anisotropy enhancement. Furthermore, using tabulated values of the magnetostriction and of the elastic coefficients, combined with the experimental values of the strain in Table I, the magnitude of $K_{\mathrm{me}}^{(1)}$ can be calculated using Eq. (1) and compared to experimental data. For Co-rich samples, we obtain values of $K_{\mathrm{me}}^{(1)}$ typically half as large as those obtained using tabulated coefficients and measured strains (40%–60%). This could in part be due to coefficients departing from their bulk values. Another, more plausible, cause of discrepancy lies in the fact that the strain is not homogeneous within the nanowires, leading to a broad distribution of anisotropy. This aspect will be addressed in the next subsection.

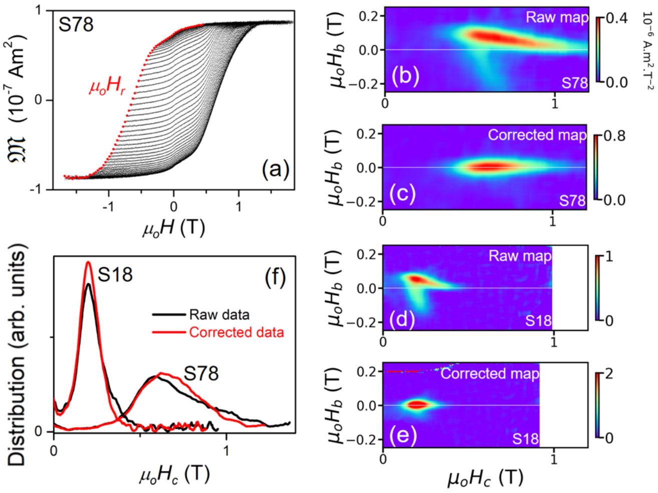

FIG. 7. Coercive field distributions in samples S78 and S18 extracted from FORC measurements at 5 K with the field applied along the axis of the nanowires. (a) Reversal curves $\mathfrak{M}(H_r, H)$ measured in sample S78, after saturation at 1.86 T prior to each reversal and with the reversal field $\mu_0 H_r$ decreasing from 0.45 to −1.68 T in steps of −0.03 T (red dotted field positions). (b) Raw and (c) dipolar effect corrected FORC maps of sample S78. (d) Raw and (e) dipolar effect corrected FORC maps of sample S18. (f) Raw (black) and intrinsic (red/gray) coercive field distributions in samples S78 and S18, obtained by integrating the FORC maps along the $\mu_0 H_c$ axis.

B. Distribution of energy barriers

In the case of uniaxial anisotropy, the energy barrier against magnetic reversal can be expressed as $K_{\mathrm{eff}} V$, where V is the activation volume and K_{eff} is the associated effective anisotropy constant. Here we analyze internal energy barriers through the distribution of coercive fields at low temperature, based on the link between K_{eff} and $\mu_0 H_{c,0}$, the coercive field at 0 K: $\mu_0 H_{c,0} = 2K_{\mathrm{eff}}/M_s$.

Figure 7(a) displays the reversal curves $\mathfrak{M}(H_r, H)$ obtained by VSM measurements in sample S78 at 5 K with the field applied along the NW axis, $\mathfrak{M}(H_r, H)$ being the magnetization measured at the field $\mu_0 H$ after saturation at 1.8 T and a reversal at H_r. The FORC map in Fig. 7(b), the mixed second-order derivatives of $\mathfrak{M}(H_r, H)$, is shown as a function of $H_c = (H - H_r)/2$ and $H_b = (H + H_r)/2$. The $\mu_0 H_c$ values represent the apparent coercive fields of subjacent hysteresis loops and the $\mu_0 H_b$ ones their bias [32,33]. The FORC map exhibits a "wishbone" structure, where the intensity is unequally distributed along the two branches. This pattern is characteristic of a dipolar-interacting NW assembly and can be understood within the framework of mean field theory [41,42]. Indeed, the local field felt by a NW results from the applied field and the dipolar field $\mu_0 H_{\mathrm{dip}}$ which is related to the actual magnetization density of the film containing the NWs via $\mu_0 H_{\mathrm{dip}} = -\mu_0 \mathfrak{M}/V_{\mathrm{film}}$ (V_{film} is the thin film volume). By adding $\mu_0 H_{\mathrm{dip}}$ to the applied fields $\mu_0 H_r$ and $\mu_0 H$, the transformed reversal curves provide a FORC map where the bias fields are subtracted and the coercive fields are intrinsic [Fig. 7(c)]. The same procedure was applied to sample S18 and the corresponding raw and corrected FORC maps were obtained as shown in Figs. 7(d) and 7(e).

Figure 7(f) displays the raw and intrinsic coercive field distributions obtained in samples S78 and S18 at 5 K. It can be seen that after subtraction of the dipolar effect, the tail of the distribution in the high $\mu_0 H_c$ part is suppressed and weight is transferred at lower $\mu_0 H_c$ values. For sample S78, the mean value of $\mu_0 H_c$ shifts from 0.71 T in the raw case to 0.67 T in the intrinsic one, while the FWHM of the distribution remains unchanged at 0.42 T. Similarly for sample S18, the mean value of $\mu_0 H_c$ decreases slightly from 0.25 to 0.24 T and the FWHM remains at 0.13 T. This indicates that dipolar effects are weak in the present case and the slopes of magnetic hysteresis cycles in the samples (Fig. 4) reflect mainly a distribution of intrinsic coercive fields, i.e., a distribution of internal energy barriers inside the NWs.

To elucidate the impact of temperature on the internal energy barrier distribution, we performed systematic T-dependent magnetic hysteresis cycle VSM measurements, as shown for sample S78 from 5 to 350 K in Fig. 8(a). This allowed us to extract $\mu_0 H_c(T)$. Figures 8(b) and 8(c) show the $\mu_0 H_c(T)$ curves for samples S78 and S18. The data are well fitted by Sharrock's formula, which describes the thermal reduction of coercive fields in the case of a temperature-independent energy barrier [43–45]:

$$\mu_0 H_c(T) = \mu_0 H_{c,0}[1 - (T/T_b)^{1/m}], \tag{2}$$

where T_b is the blocking temperature and $m = 3/2$. The values of T_b found are equal to 623 K for sample S78 and 197 K for sample S18. In addition, supplementary FORC measurements were performed in sample S78 at 100 and 200 K, in order to observe thermal variations of the coercive field distribution. The FWHMs of the distributions are equal to 0.42, 0.29, and 0.22 T at 5, 100, and 200 K, respectively. These values also follow Sharrock's thermal reduction formula [Eq. (2)]. This means that not only the mean energy barrier but also the whole distribution of internal energy barriers is stable in the temperature range of the measurements. This result reinforces the idea that internal energy barriers in the NWs are related to the magnetostatic (shape) and magnetoelastic (strain) anisotropies that do not depend sensitively on the temperature.

The thermal evolution of the magnetic cycles provides key characteristics of the NWs: T_b, $\mu_0 H_{c,0}$, as well as K_{eff}. Furthermore, the distributions of intrinsic coercive fields, extracted from the FORC measurements at 5 K [Fig. 7(f)], can be read in the scale of $\mu_0 H_{c,0}$ and then of K_{eff}, giving also the mean value of K_{eff} and the FWHM of the K_{eff} distribution. The results obtained for samples S18 and S78 are summarized in Table III.

Given the smallness of NW diameters d, the magnetization can be considered coherent in a NW section of volume equal to the activation volume V. An activation length L can then be deduced from V by considering that $V = \pi(d/2)^2 L$. The blocking temperature T_b provides a direct estimation of the activation length L. According to the Néel-Brown theory [46], using a typical measurement duration of 1 s, the following criterion is generally used to account for the balance between the thermal activation and an energy barrier of $K_{\text{eff}}V$: $25k_B T_b = K_{\text{eff}}V$ (k_B: Boltzmann constant). The activation lengths L thus deduced are 39 nm in sample S18 and 25 nm in samples S78 (Table III), which suggests a localized magnetization reversal mechanism. Indeed, unlike for a coherent Stoner-Wohlfarth reversal [47], the coercive fields $H_{c,0}$ are much smaller than

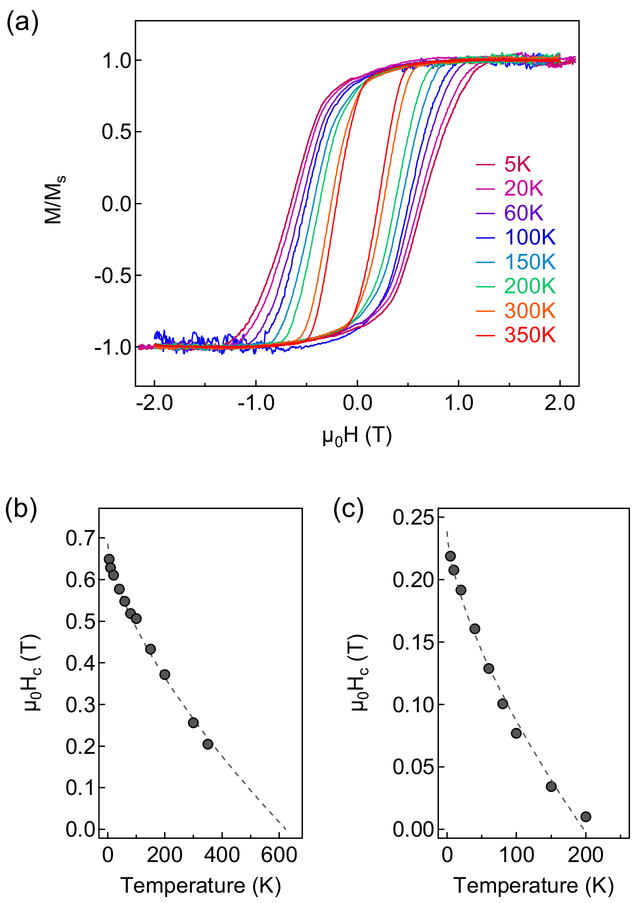

FIG. 8. Thermal evolution of magnetic hysteresis cycles measured by VSM. (a) Cycles from 5 to 350 K of sample S78, with the applied field along the nanowire axis. (b) Thermal evolution of the coercive field $\mu_0 H_c$ in sample S78 (dots). The line is a fit to Sharrock's formula [Eq. (2)], with $T_b = 623$ K. (c) Same as (b) for sample S18, with $T_b = 197$ K.

TABLE III. Mean characteristics deduced from the cycles $M(H)$ and the FORC measurements in samples S18 and S78. Meas., $M(H)$, and FORC-related values are labeled by $M(H)$ and FORC, respectively; T_b, blocking temperature; $\mu_0 H_{c,0}$, coercive field at 0 K; K_{eff}, effective anisotropy constant; $W_{K_{\text{eff}}}$, FWHM of the K_{eff} distribution; δ_0, domain wall width; L, activation length.

Sample	Meas.	T_b (K)	$\mu_0 H_{c,0}$ (T)	K_{eff} (J/m^3)	$W_{K_{\text{eff}}}$ (J/m^3)	δ_0 (nm)	L (nm)
S18	$M(H)$	197	0.24	0.8×10^5		39	39
	FORC		0.26	0.9×10^5	0.5×10^5	37	
S78	$M(H)$	623	0.69	4.3×10^5		23	25
	FORC		0.70	4.3×10^5	2.7×10^5	23	

the anisotropy fields H_a that are determined by the saturation fields in the hard plane $H_s^{\perp}$ (Sec. IV A). In the present system, L is generally much smaller than the total physical length of the NWs and interestingly very close to the Bloch domain wall widths δ_0 ($\delta_0 = \pi\sqrt{A/K_{\mathrm{eff}}}$, with A the exchange stiffness constant). This indicates that the magnetization reversal in the NWs is initiated by creation of a domain wall. The result is consistent with the general idea that magnetization reversal should be localized in a NW, initiated by morphological, structural, or anisotropy inhomogeneities and nucleated over the length of a domain wall [19,48,49].

We now turn to the analysis of the distribution of internal energy barriers, linking them with the wide strain distribution observed in our XRD data. In all samples, a broad 002 peak in θ-2θ scans was measured, see Fig. 3(b). This corresponds to a large FWHM ($W_{\epsilon_{zz}}$) of the ϵ_{zz} distribution that is equal to 3%–4% and of the same order of magnitude as $\langle\epsilon_{zz}\rangle$. Such a wide strain distribution implies a large FWHM of K_{eff} through the magnetoelastic term: $W_{K_{\mathrm{eff}}} = (3/2)\lambda_{001}(c_{11} - c_{12})W_{\epsilon_{zz}}$. The expected values of $W_{K_{\mathrm{eff}}}$ are 0.7×10^5 and 10.3×10^5 J/m^3 for samples S18 and S78, respectively. In the case of sample S18, the narrow distribution of coercive fields observed [Fig. 7(f)] is compatible with the expected value: the measured value $W_{K_{\mathrm{eff}}} = 0.5 \times 10^5$ J/m^3 is quite close to the calculated one. It should be recalled that at 20% of Co content, the magnetostriction constant λ_{001} is close to zero [13] and the magnetoelastic effect vanishes. However, in the case of sample S78, the measured width $W_{K_{\mathrm{eff}}} = 2.7 \times 10^5$ J/m^3 is almost four times smaller than the calculated one.

The mean values and the FWHMs of anisotropy constants (K_{eff} and $W_{K_{\mathrm{eff}}}$) deduced from magnetic measurements were also lower than those predicted from strain using Eq. (1) for the other samples. We postulate that the observed discrepancy could find an explanation by considering not directly the strain distribution but a strain distribution averaged over the activation length. A structural study of similar Ni NWs using synchrotron radiation-based XRD has shown that NWs are composed of domains of structural coherence length ranging from 6 to 13 nm, the domains having the longer coherence length being strained to a lesser extent [30]. Activation lengths for the magnetization reversal fall in the 20–40 nm range (cf. values of δ_0 in Table III). Therefore, the structural coherence length, which is the characteristic length for homogeneous strain, is smaller that the magnetic characteristic length. Thus, averaging should be performed over several structural domains. This would lead to values of K_{eff} and $W_{K_{\mathrm{eff}}}$ that are substantially smaller than the one obtained when considering $\langle\epsilon_{zz}\rangle$ and $W_{\epsilon_{zz}}$ values in Eq. (1).

C. Spin and orbital moments

Having established the central role played by magnetoelastic anisotropy contributions in CoNi-SrTiO$_3$ VANs, we now address the microscopic origin of the latter by relying on a quantitative analysis of XAS and XMCD data. Figure 9 shows XAS and XMCD spectra of sample S78 at $T = 4.2$ K. The XAS spectra, characteristic of metallic Co and Ni, indicate

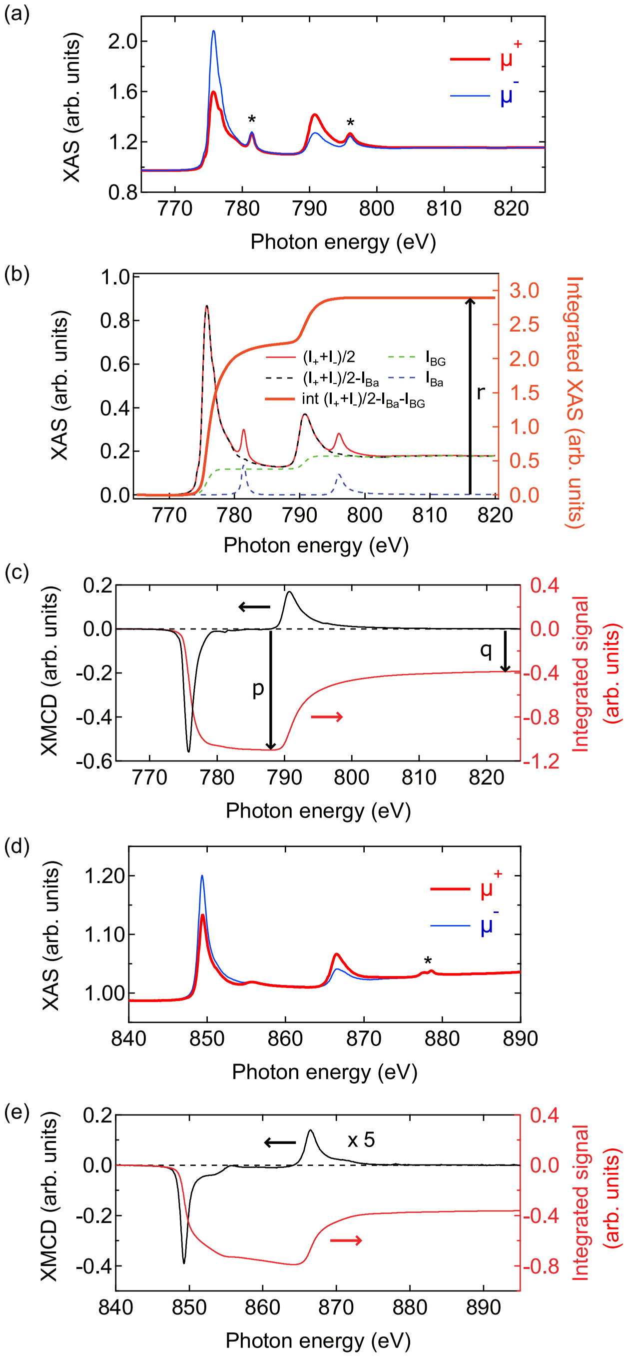

FIG. 9. XAS and XMCD spectra acquired at $T = 4.2$ K and $\gamma = 0$ at the Co and Ni $L_{2,3}$ edges on sample S78. (a) XAS spectra for μ^+ and μ^- configurations at the Co $L_{2,3}$ edges. The peaks marked by asterisks are due to Ba impurities in the SrTiO$_3$ matrix. (b) Averaged XAS spectrum (background corrected) and its integral after Ba contribution (I_{Ba}) and background (I_{BG}) removal. (c) XMCD at the Co $L_{2,3}$ edges. Black line: spectrum, red (gray) line: integrated signal. Note that the spectral features related to Ba in XAS do not give rise to any significant dichroic signal. (d) XAS spectra for μ^+ and μ^- configurations at the Ni $L_{2,3}$ edges. The peak marked by an asterisk is due to Ce impurities in the SrTiO$_3$ matrix. (e) XMCD at the Ni $L_{2,3}$ edges. Black line: Spectrum. Red (gray) line: Integrated signal.

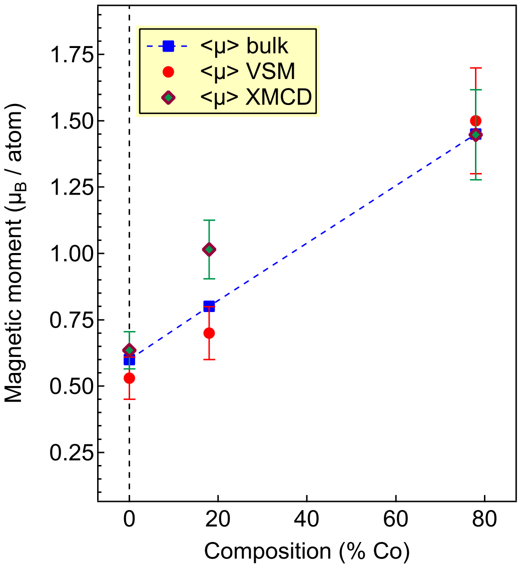

FIG. 10. Average magnetic moment $\langle\mu\rangle$ for S00, S18, and S78 samples, as measured by VSM (disks) and XMCD using Eq. (5) (diamonds). Squares: Bulk values.

the absence of detectable oxidation of the transition metals in the nanowires. This is in agreement with earlier spectromicroscopy studies that unraveled sharp metal/oxide interfaces in Ni-SrTiO$_3$ VANs [11].

XMCD spectra, such as the ones shown in Figs. 9(c) and 9(e), were recorded for samples S00, S18, and S78 for distinct values of the angle γ in the 0–45 deg range. Application of the XMCD sum rules [14,15] allowed us to extract values of the orbital moment m_l and effective spin moment m_s^{eff}. We define p, q, and r as the integrated XMCD signal at the L_3 edge, the integrated XMCD signal at the L_2 edge, and the integrated XAS intensity after background removal, respectively. The values of these integrals are symbolized by arrows in Figs. 9(b) and 9(c). m_l and m_s^{eff} can be calculated from p, q, and r by using the following equations:

$$m_l = -\frac{2q}{3r} n_h \mu_B, \tag{3}$$

$$m_s^{\text{eff}} = -\frac{3p - 2q}{r} n_h \mu_B. \tag{4}$$

Here n_h is the number of holes in the d band, and $\mu_B = +9.274\,010\,0783(28)\,10^{-24}$ J T^{-1} is the Bohr magneton. Using the XMCD sum rules, the average magnetic moment per atom $\langle\mu\rangle$ in the Co$_x$Ni$_{1-x}$ alloys can be determined as

$$\langle\mu\rangle = x\big(m_s^{\text{eff,Co}} + m_l^{\text{Co}}\big) + (1-x)\big(m_s^{\text{eff,Ni}} + m_l^{\text{Ni}}\big). \tag{5}$$

The results are displayed in Fig. 10 where $\langle\mu\rangle$ is compared to values extracted by VSM measurements and to the bulk values. The agreement between these values is good, except for the S18 sample with a larger moment, which might be due to Ba corrections in this case. It should be noted that we used $n_h = 1$ for Ni and $n_h = 2$ for Co which are the lowest possible values for the number of holes in the 3d band. Such values are significantly smaller than those commonly employed (e.g., 1.45 for Ni [50]).

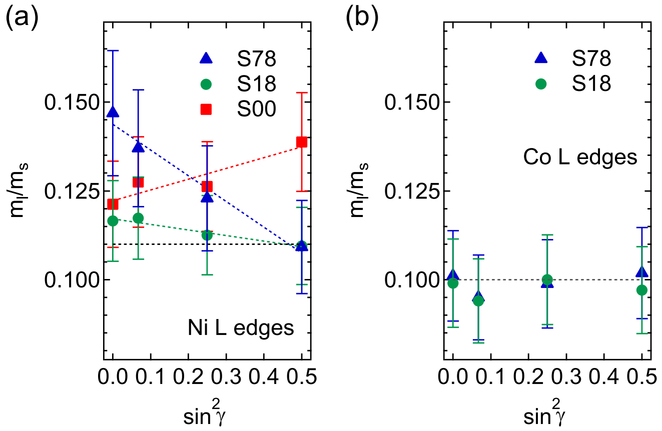

FIG. 11. m_l/m_s ratio, extracted from XMCD data by application of the sum rules, as a function of $\sin^2\gamma$ for samples S00, S18, and S78. (a) m_l/m_s ratio at Ni $L_{2,3}$ edges, (b) m_l/m_s ratio at Co $L_{2,3}$ edges. Black horizontal dashed line: Bulk value.

m_l/m_s^{eff}, the ratio of orbital moment over effective spin moment, can be extracted without any assumptions on unknown parameters such as n_h the d-band occupancy. The angular dependence of m_l/m_s^{eff} for samples with different concentrations is shown in Fig. 11. Note that no electron yield saturation corrections were used in our calculations [51], as expected from the measured thickness of the samples compared to the penetration depth of the x rays.

At the Ni $L_{2,3}$ edges, the m_l/m_s^{eff} ratio is systematically larger than the one of bulk Ni [52]. Furthermore, the variation of m_l/m_s^{eff} with $\sin^2\gamma$ is not the same for all the samples probed: for S00 (pure Ni), m_l/m_s^{eff} increases with $\sin^2\gamma$, it is roughly constant for S18 and it decreases with $\sin^2\gamma$ for S78. In contrast, the values of m_l/m_s^{eff} for Co are constant when $\sin^2\gamma$ varies and match well with the value of bulk Co [53].

m_l and m_s^{eff} can be expressed as a function of $\sin^2\gamma$ as follows [54]:

$$m_l = m_l^0 - \Delta m_l \sin^2\gamma, \tag{6}$$

$$m_s^{\text{eff}} = m_s + 7T_z. \tag{7}$$

In these equations, Δm_l accounts for the anisotropy of m_l, m_l^0 is the orbital magnetic moment for $\gamma = 0$, and T_z is the expectation value for the spin magnetic dipole operator. For a transition metal, Stöhr and König demonstrated that the effect of the spin-orbit coupling on the magnetic dipolar term is weak [55]. We suppose that the angular variation of m_s^{eff} is entirely contained by T_z that varies similarly to the orbital moment with $\sin^2\gamma$. Then, for a 3d metal with uniaxial symmetry, T_z can be expressed as an affine function of $\sin^2\gamma$: $T_z = 14Q_{xx} - 21Q_{xx}\sin^2\gamma$ [56–58]. In the present case we did not measure any clear anisotropy of m_s^{eff}. From the preceding equations, it follows that the approximation $T_z \ll m_s$ is valid in the systems probed here. Therefore, we have $m_s^{\text{eff}} \simeq m_s$, independent of $\sin^2\gamma$ and the variation of m_l/m_s^{eff} reflects the anisotropy of the orbital moment and is directly related to Δm_l.

The anisotropy of the orbital moment can be linked to the uniaxial magnetic anisotropy in the framework of a microscopic model developed by Bruno [16]. Such an approach has been used previously in the case of ultrathin films of 3d metals [58,59]. According to Bruno's model, the uniaxial magnetic anisotropy $K_u^{(1)}$ is directly linked to the anisotropy of the orbital moment through

$$K_u^{(1)} = \alpha \frac{N}{V} \xi \frac{\Delta \mu_l}{4\mu_B}. \tag{8}$$

In this equation, $\frac{N}{V}$ is the atomic density, ξ is the spin-orbit coupling parameter, μ_B is the Bohr magneton, and α is a prefactor, which depends on the electronic band structure.

Our measurements illustrate that the variations of the orbital moment of Ni with $\sin^2 \gamma$ are consistent with the expected uniaxial magnetoelastic anisotropy: $K_{\mathrm{me}}^{(1)}$ should be negative for pure Ni, corresponding to a positive slope of $m_l(\sin^2 \gamma)$, it should be positive for S78 with a negative slope of $m_l(\sin^2 \gamma)$, and very weak around 20% Co with no angular variation of m_l. This is exactly what we observe for measurements performed at the Ni $L_{2,3}$ edges, as shown in Fig. 11. In the case of pure Ni, taking the value from the literature for ξ (105 meV [60]) and the bulk value of m_s, the estimated value of $K_u^{(1)}$ using Eq. (8) is in agreement with the one estimated by cyclic magnetometry [12] if α is taken equal to 0.016. Interestingly, such a value is smaller than the ones obtained using the same approach in thin films with typical α values reported so far varying between 0.05 and 1 [61–63].

No anisotropy effects are evidenced at the Co L edge: no angular dependence is observed and m_l/m_s remains close to the bulk value. The absence of anisotropy of the orbital moment of Co, within the precision of our measurements, is in contrast with the large orbital moment enhancement and angular variations observed at the Ni $L_{2,3}$ edges. A simple explanation is still missing, but clearly this issue deserves further investigation.

V. CONCLUSION

In the present work we have studied the magnetic properties of VANs hosting $\mathrm{Co}_x\mathrm{Ni}_{1-x}$ nanowires with diameters in the 3–5 nm range through a combination of XMCD spectroscopy and extraction magnetometry experiments. The large axial strain present in the $\mathrm{Co}_x\mathrm{Ni}_{1-x}$ nanowires, as determined by x-ray diffraction, leads to a sizable magnetoelastic anisotropy that reinforces the total uniaxial anisotropy of the system for $x > 0.2$. This leads to an increase in the blocking temperature that exceeds 600 K in the case of 5 nm wires with 78% Co content.

The values of the magnetic moment were deduced by analysis of the XMCD measurements at the Ni and Co L edges using sum rules. The obtained moment values are in agreement with the one measured by extraction magnetometry. The anisotropy of the orbital moment was also studied. Surprisingly, while a significative anisotropy of the Ni orbital moment is found, no such anisotropy is observed for Co.

Finally, it should be noted that the enhancement of the uniaxial anisotropy of the VANs is less pronounced than the one calculated using an homogeneous axial strain equal to the measured mean value $\langle \epsilon_{zz} \rangle$. This is due to the inhomogeneity of the axial strain. Future work on the impact of structural disorder on the magnetic properties may allow for further optimization of the magnetic properties of these metal-oxide VANs.

ACKNOWLEDGMENTS

The authors acknowledge SOLEIL synchrotron for granting beam time (Proposal No. 20171138). The authors also gratefully thank M. Sacchi for discussions, N. Casaretto for diffraction measurements, F. Breton for his assistance and design of the PLD control system, Ch. Hébert for his help with the laser system, the staff of the MPBT platform of Sorbonne Université for their support, J.-M. Guigner for assistance with TEM measurements, and IMPMC for access to the TEM facilities. Xiaorong Weng gratefully acknowledges financial support of the Chinese Government Scholarship from China Scholarship Council (CSC No. 201608070062). This work was supported by French state funds managed by the Agence Nationale de la Recherche within the Investissements d'Avenir programme under reference ANR-11-IDEX-0004-02, and more specifically within the framework of the Cluster of Excellence MATISSE led by Sorbonne Universités. This work has benefited from funding from LabEx PALM (ANR-10-LABX-0039-PALM). M. Hennes acknowledges financial support from the French Embassy in Berlin (Service pour la Science et la Technologie) and Campus France.

---

[1] C. A. F. Vaz, J. A. C. Bland, and G. Lauhoff, Rep. Prog. Phys. **71**, 056501 (2008).

[2] A. Chen and Q. Xia, MRS Bull. **46**, 115 (2021).

[3] H. Zheng, J. Wang, S. E. Lofland, Z. Ma, L. Mohaddes-Ardabili, T. Zhao, L. Salamanca-Riba, S. R. Shinde, S. B. Ogale, F. Bai, D. Viehland, Y. Jia, D. G. Schlom, M. Wuttig, A. Roytburd, and R. Ramesh, Science **303**, 661 (2004).

[4] N. Dix, R. Muralidharan, J.-M. Rebled, S. Estradé, F. Peiró, M. Varela, J. Fontcuberta, and F. Sánchez, ACS Nano **4**, 4955 (2010).

[5] N. M. Aimon, D. H. Kim, H. K. Choi, and C. A. Ross, Appl. Phys. Lett. **100**, 092901 (2012).

[6] Z. Wang, R. Viswan, B. Hu, V. G. Harris, J.-F. Li, and D. Viehland, Phys. Status Solidi RRL **6**, 92 (2012).

[7] H.-J. Liu, Y.-Y. Liu, C.-Y. Tsai, S.-C. Liao, Y.-J. Chen, H.-J. Lin, C.-H. Lai, W.-F. Hsieh, J.-Y. Li, C.-T. Chen, Q. He, and Y.-H. Chu, Sci. Rep. **5**, 12073 (2015).

[8] T. O. Farmer, E.-J. Guo, R. D. Desautels, L. De Beer-Schmitt, A. Chen, Z. Wang, Q. Jia, J. A. Borchers, D. A. Gilbert, B. Holladay, S. K. Sinha, and M. R. Fitzsimmons, Phys. Rev. Materials **3**, 081401(R) (2019).

[9] M. Hennes, D. Demaille, G. Patriarche, T. Tran, Y. Zheng, and F. Vidal, MRS Bull. **46**, 136 (2021).

[10] S. Misra and H. Wang, Mater. Horiz. **8**, 869 (2021).

[11] G. Radtke, M. Hennes, M. Bugnet, Q. Ramasse, X. Weng, D. Demaille, B. Gobaut, P. Ohresser, E. Otero, F. Choueikani, A. Juhin, Ph. Sainctavit, Y. Zheng, and F. Vidal, Adv. Mater. Interfaces **6**1900549 (2019).

[12] X. Weng, M. Hennes, D. Hrabovsky, D. Demaille, F. Vidal, and Y. Zheng, J. Magn. Magn. Mater. **501**, 166375 (2020).

[13] R. C. Hall, J. Appl. Phys. **30**, 816 (1959).

[14] B. T. Thole, P. Carra, F. Sette, and G. van der Laan, Phys. Rev. Lett. **68**, 1943 (1992).

[15] P. Carra, B. T. Thole, M. Altarelli, and X. Wang, Phys. Rev. Lett. **70**, 694 (1993).

[16] P. Bruno, Phys. Rev. B **39**, 865 (1989).

[17] F. Vidal, Y. Zheng, J. Milano, D. Demaille, P. Schio, E. Fonda, and B. Vodungbo, Appl. Phys. Lett. **95**, 152510 (2009).

[18] P. Schio, F. Vidal, Y. Zheng, J. Milano, E. Fonda, D. Demaille, B. Vodungbo, J. Varalda, A. J. A. de Oliveira, and V. H. Etgens, Phys. Rev. B **82**, 094436 (2010).

[19] F. Vidal, Y. Zheng, P. Schio, F. J. Bonilla, M. Barturen, J. Milano, D. Demaille, E. Fonda, A. J. A. de Oliveira, and V. H. Etgens, Phys. Rev. Lett. **109**, 117205 (2012).

[20] P. Schio, F. J. Bonilla, Y. Zheng, D. Demaille, J. Milano, A. J. A. de Oliveira, and F. Vidal, J. Phys.: Condens. Matter **25**, 056002 (2013).

[21] P. Schio, M. Barturen, J. Milano, F. J. Bonilla, Y. Zheng, F. Vidal, and A. J. A. de Oliveira, Mater. Res. Express **1**, 035015 (2014).

[22] A. Novikova, E. Fonda, Y. Dumont, Y. Zheng, D. Demaille, and F. Vidal, J. Phys. D: Appl. Phys. **48**, 235001 (2015).

[23] F. J. Bonilla, A. Novikova, F. Vidal, Y. Zheng, E. Fonda, D. Demaille, V. Schuler, A. Coati, A. Vlad, Y. Garreau, M. Sauvage-Simkin, Y. Dumont, S. Hidki, and V. H. Etgens, ACS Nano **7**, 4022 (2013).

[24] V. Schuler, F. J. Bonilla, D. Demaille, A. Coati, A. Vlad, Y. Garreau, M. Sauvage-Simkin, A. Novikova, E. Fonda, S. Hidki, V. Etgens, F. Vidal, and Y. Zheng, Nano Res. **8**, 1964 (2015).

[25] V. Schuler, J. Milano, A. Coati, A. Vlad, M. Sauvage-Simkin, Y. Garreau, D. Demaille, S. Hidki, A. Novikova, E. Fonda, Y. Zheng, and F. Vidal, Nanotechnology **27**, 495601 (2016).

[26] M. Hennes, V. Schuler, X. Weng, J. Buchwald, D. Demaille, Y. Zheng, and F. Vidal, Nanoscale **10**, 7666 (2018).

[27] A. A. Stashkevich, Y. Roussigné, A. N. Poddubny, S.-M. Chérif, Y. Zheng, F. Vidal, I. V. Yagupov, A. P. Slobozhanyuk, P. A. Belov, and Y. S. Kivshar, Phys. Rev. B **92**, 214436 (2015).

[28] Y. Roussigné, S. M. Chérif, A. A. Stashkevich, F. Vidal, and Y. Zheng, J. Appl. Phys. **118**, 233903 (2015).

[29] Y. Roussigné, A. Stashkevich, S.-M. Chérif, F. Vidal, Y. Zheng, and A. Starkov, Phys. Rev. B **100**, 134406 (2019).

[30] X. Weng, M. Hennes, A. Coati, A. Vlad, Y. Garreau, M. Sauvage-Simkin, E. Fonda, G. Patriarche, D. Demaille, F. Vidal, and Y. Zheng, Phys. Rev. Materials **2**, 106003 (2018).

[31] M. Hennes, X. Weng, E. Fonda, B. Gallas, G. Patriarche, D. Demaille, Y. Zheng, and F. Vidal, Phys. Rev. Materials **3**, 035002 (2019).

[32] C. R. Pike, Phys. Rev. B **68**, 104424 (2003).

[33] R. J. Harrison and J. M. Feinberg, Geochem. Geophys. Geosyst. **9**, n/a (2008).

[34] P. Ohresser, E. Otero, F. Choueikani, K. Chen, S. Stanescu, F. Deschamps, T. Moreno, F. Polack, B. Lagarde, J.-P. Daguerre, F. Marteau, F. Scheurer, L. Joly, J.-P. Kappler, B. Muller, O. Bunau, and Ph. Sainctavit, Rev. Sci. Instrum. **85**, 013106 (2014).

[35] L. Joly, E. Otero, F. Choueikani, F. Marteau, L. Chapuis, and P. Ohresser, J. Synchrotron Radiat. **21**, 502 (2014).

[36] J.-P. Kappler, E. Otero, W. Li, L. Joly, G. Schmerber, B. Muller, F. Scheurer, F. Leduc, B. Gobaut, L. Poggini, G. Serrano, F. Choueikani, E. Lhotel, A. Cornia, R. Sessoli, M. Mannini, M.-A. Arrio, Ph. Sainctavit, and P. Ohresser, J. Synchrotron Radiat. **25**, 1727 (2018).

[37] X. Weng, M. Hennes, T. Tran, N. Casaretto, D. Demaille, F. Vidal, and Y. Zheng, CrystEngComm **22**, 4730 (2020).

[38] T. Suzuki, Y. Nishi, and M. Fujimoto, Philos. Mag. A **80**, 621 (2000).

[39] T. Ohnishi, K. Shibuya, T. Yamamoto, and M. Lippmaa, J. Appl. Phys. **103**, 103703 (2008).

[40] C. M. Brooks, L. F. Kourkoutis, T. Heeg, J. Schubert, D. A. Muller, and D. G. Schlom, Appl. Phys. Lett. **94**, 162905 (2009).

[41] C. R. Pike, C. A. Ross, R. T. Scalettar, and G. Zimanyi, Phys. Rev. B **71**, 134407 (2005).

[42] S. Ruta, O. Hovorka, P.-W. Huang, K. Wang, G. Ju, and R. Chantrell, Sci. Rep. **7**, 45218 (2017).

[43] M. P. Sharrock, J. Appl. Phys. **76**, 6413 (1994).

[44] R. Skomski, D. Leslie-Pelecky, R. D. Kirby, A. Kashyap, and D. J. Sellmyer, Scr. Mater. **48**, 857 (2003).

[45] O. Fruchart and A. Thiaville, C. R. Phys. **6**, 921 (2005).

[46] W. F. Brown Jr., Phys. Rev. **130**, 1677 (1963).

[47] E. C. Stoner and E. P. Wohlfarth, Philos. Trans. R. Soc. London Sect. A **240**, 599 (1948).

[48] R. Skomski, H. Zeng, M. Zheng, and D. J. Sellmyer, Phys. Rev. B **62**, 3900 (2000).

[49] M. I. Chipara, R. Skomski, and D. J. Sellmyer, J. Magn. Magn. Mater. **249**, 246 (2002).

[50] P. Srivastava, N. Haack, H. Wende, R. Chauvistré, and K. Baberschke, Phys. Rev. B **56**, 4398(R) (1997).

[51] R. Nakajima, J. Stöhr, and Y. U. Idzerda, Phys. Rev. B **59**, 6421 (1999).

[52] J. Vogel, G. Panaccione, and M. Sacchi, Phys. Rev. B **50**, 7157 (1994).

[53] C. T. Chen, Y. U. Idzerda, H.-J. Lin, N. V. Smith, G. Meigs, E. Chaban, G. H. Ho, E. Pellegrin, and F. Sette, Phys. Rev. Lett. **75**, 152 (1995).

[54] G. van der Laan, J. Phys.: Condens. Matter **10**, 3239 (1998).

[55] J. Stöhr and H. König, Phys. Rev. Lett. **75**, 3748 (1995).

[56] P. Ohresser, N. B. Brookes, S. Padovani, F. Scheurer, and H. Bulou, Phys. Rev. B **64**, 104429 (2001).

[57] H. A. Dürr and G. van der Laan, Phys. Rev. B **54**, R760 (1996).

[58] S. Andrieu, T. Hauet, M. Gottwald, A. Rajanikanth, L. Calmels, A. M. Bataille, F. Montaigne, S. Mangin, E. Otero, P. Ohresser, P. Le Fèvre, F. Bertran, A. Resta, A. Vlad, A. Coati, and Y. Garreau, Phys. Rev. Materials **2**, 064410 (2018).

[59] J. M. Shaw, H. T. Nembach, and T. J. Silva, Phys. Rev. B **87**, 054416 (2013).

[60] G. H. O. Daalderop, P. J. Kelly, and M. F. H. Schuurmans, Phys. Rev. B **41**, 11919 (1990).

[61] D. Weller, J. Stohr, R. Nakajima, A. Carl, M. G. Samant, C. Chappert, R. Megy, P. Beauvillain, P. Veillet, and G. A. Held, Phys. Rev. Lett. **75**, 3752 (1995).

[62] F. Wilhelm, P. Poulopoulos, P. Srivastava, H. Wende, M. Farle, K. Baberschke, M. Angelakeris, N. K. Flevaris, W. Grange, J.-P. Kappler, G. Ghiringhelli, and N. B. Brookes, Phys. Rev. B **61**, 8647 (2000).

[63] O. Hjortstam, K. Baberschke, J. M. Wills, B. Johansson, and O. Eriksson, Phys. Rev. B **55**, 15026 (1997).